

Topological insulators in twisted transition metal dichalcogenide homobilayers

Fengcheng Wu,^{1,2} Timothy Lovorn,³ Emanuel Tutuc,⁴ Ivar Martin,¹ and A. H. MacDonald³

¹Materials Science Division, Argonne National Laboratory, Argonne, Illinois 60439, USA

²Condensed Matter Theory Center and Joint Quantum Institute,

Department of Physics, University of Maryland, College Park, Maryland 20742, USA

³Department of Physics, University of Texas at Austin, Austin, Texas 78712, USA

⁴Department of Electrical and Computer Engineering, Microelectronics Research Center, The University of Texas at Austin, Austin, Texas 78758, USA

We show that moiré bands of twisted homobilayers can be topologically nontrivial, and illustrate the tendency by studying valence band states in $\pm K$ valleys of twisted bilayer transition metal dichalcogenides, in particular, bilayer MoTe₂. Because of the large spin-orbit splitting at the monolayer valence band maxima, the low energy valence states of the twisted bilayer MoTe₂ at $+K$ ($-K$) valley can be described using a two-band model with a layer-pseudospin magnetic field $\Delta(\mathbf{r})$ that has the moiré period. We show that $\Delta(\mathbf{r})$ has a topologically non-trivial skyrmion lattice texture in real space, and that the topmost moiré valence bands provide a realization of the Kane-Mele quantum spin-Hall model, i.e., the two-dimensional time-reversal-invariant topological insulator. Because the bands narrow at small twist angles, a rich set of broken symmetry insulating states can occur at integer numbers of electrons per moiré cell.

Introduction.— Moiré superlattices form in van der Waals bilayers with small differences between the lattice constants or orientations of the individual layers, and often dramatically alter electronic properties [1–6]. In the presence of long-period moiré patterns, electronic states can be described by continuum model Hamiltonians with the moiré periodicity and spinors whose dimension is equal to the total number of bands, summed over layers, in the energy range of interest. Application of Bloch’s theorem then gives rise to moiré bands [7]. Because the moiré pattern often generates spatial confinement, moiré bands can be narrow, enhancing the importance of electronic correlations. The flat bands of magic-angle twisted bilayer graphene, in which correlated insulating and superconducting states have been discovered [8, 9], provide a prominent example. The study of moiré flat bands has recently become an active area of experimental and theoretical research centered on efforts to identify promising bilayer structures, and on topological characterization and many-body interaction physics [10–15].

When the two layers are formed from the same material (homobilayers), both must be treated on an equal footing. The $\pm K$ -valley valence bands of semiconductor group-VI transition metal dichalcogenide (TMD) monolayers provide a prototypical model system because strong spin-orbit coupling and broken inversion symmetry lifts spin-degeneracy [16], and the corresponding homobilayer can be described by a two-band model with layer pseudospins at each valley. The moiré pattern’s periodic modulation can then be accounted for by a scalar potential and a pseudo magnetic field $\Delta(\mathbf{r})$ whose components are the coefficients of the layer Pauli matrix expansion of the two-band Hamiltonian, i.e. Δ_x and Δ_y are the real and imaginary parts of the interlayer tunneling amplitude and Δ_z is the potential difference between layers. The field $\Delta(\mathbf{r})$ inherits the moiré pattern periodicity

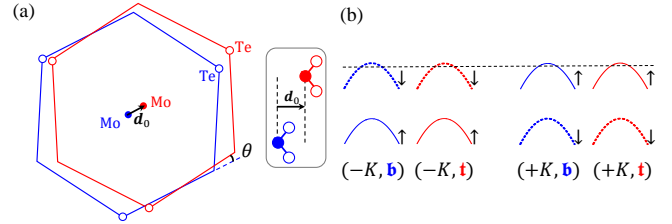


FIG. 1. (a) Top view of AA stacked MoTe₂ homobilayer with a small twist angle θ and an in-plane displacement \mathbf{d}_0 . The inset is a schematic side view. (b) $\pm K$ valence bands in the AA stacking case when interlayer coupling is neglected.

and plays a key role in the discussion below.

In this Letter, we focus on the MoTe₂ bilayer with AA stacking [Fig. 1], for which valence band maxima are located in $\pm K$ valleys according to our first-principles calculations as shown in the Supplemental Material (SM) [17]. For this system, we find that $\Delta(\mathbf{r})$ has a skyrmion lattice texture in real space, and that the moiré bands carry valley-contrasting Chern numbers. The topological moiré bands can provide a realization of the Kane-Mele model, where the effective gauge potential is generated by the momentum shift between the two twisted layers. When the bilayer is polarized by a vertical displacement potential, the band Chern numbers are driven to zero before $\Delta(\mathbf{r})$ becomes topologically trivial in real space. In partially filled topological flat bands, interactions can, for example, break time-reversal symmetry to form quantum anomalous Hall states.

Aligned bilayers— To derive a moiré continuum Hamiltonian, we start by analyzing the electronic structure of an aligned bilayer [18]. Because the $\pm K$ valleys are related by time-reversal symmetry \hat{T} , we can focus on the $+K$ valley. In an AA stacked TMD homobilayer [Fig. 1], the valence states at the $+K$ valley valence band maxi-

num are mainly of $d_{x^2-y^2} + id_{xy}$ orbital character, have spin up (\uparrow) along \hat{z} axis [16], and are separated from spin-down (\downarrow) states by strong spin-orbit splitting. Retaining only the spin up valence-band states at the $+K$ valley yields the two-band $k \cdot p$ Hamiltonian [17],

$$\mathcal{H}_\uparrow(\theta = 0, \mathbf{d}_0) = \begin{pmatrix} -\frac{\hbar^2 \mathbf{k}^2}{2m^*} + \Delta_{\mathbf{b}}(\mathbf{d}_0) & \Delta_T(\mathbf{d}_0) \\ \Delta_T^\dagger(\mathbf{d}_0) & -\frac{\hbar^2 \mathbf{k}^2}{2m^*} + \Delta_{\mathbf{t}}(\mathbf{d}_0) \end{pmatrix}, \quad (1)$$

with parameters that depend on the displacement \mathbf{d}_0 between the aligned layers. In Eq. (1), \mathbf{b} and \mathbf{t} refer to bottom (\mathbf{b}) and top (\mathbf{t}) layers, \mathbf{k} is momentum measured from $+K$ point, m^* is the valence band effective mass that is approximately independent of \mathbf{d}_0 [17], $\Delta_{\mathbf{b},\mathbf{t}}$ are layer-dependent energies, and Δ_T is an inter-layer tunneling amplitude. The dependence of Δ_α ($\alpha = \mathbf{b}, \mathbf{t}, T$) on \mathbf{d}_0 is constrained by the symmetry properties of the bilayer. The two-dimensional lattice periodicity of the aligned bilayers implies that the Δ_α are periodic functions of \mathbf{d}_0 . A $z \leftrightarrow -z$ mirror operation interchanges \mathbf{b} and \mathbf{t} and maps displacement \mathbf{d}_0 to $-\mathbf{d}_0$, implying that $\Delta_{\mathbf{t}}(\mathbf{d}_0) = \Delta_{\mathbf{b}}(-\mathbf{d}_0)$. Threefold rotation around the \hat{z} axis requires that $\Delta_{\mathbf{b}}$ and $\Delta_{\mathbf{t}}$ be invariant when \mathbf{d}_0 is rotated by $2\pi/3$. These symmetry constraints lead to the following two-parameter lowest-harmonic parametrization:

$$\Delta_\ell(\mathbf{d}_0) = 2V \sum_{j=1,3,5} \cos(\mathbf{G}_j \cdot \mathbf{d}_0 + \ell\psi), \quad (2)$$

where $\ell = 1$ for the \mathbf{b} layer and $\ell = -1$ for the \mathbf{t} layer, \mathbf{G}_j is the reciprocal lattice vector obtained by counterclockwise rotation of $\mathbf{G}_1 = (4\pi)/(\sqrt{3}a_0)\hat{y}$ by angle $(j-1)\pi/3$, a_0 is the monolayer TMD lattice constant, and V and ψ respectively characterize the amplitude and shape of the potentials. Note that we have chosen the spatial averages of $\Delta_{\mathbf{b},\mathbf{t}}$, which must be identical, as the zero of energy.

The \mathbf{d}_0 dependence of Δ_T is most conveniently understood by assuming a two-center approximation [7] for tunneling between the metal $d_{x^2-y^2} + id_{xy}$ orbitals, and using a lowest-harmonic approximation. This leads to,

$$\Delta_T(\mathbf{d}_0) = w(1 + e^{-i\mathbf{G}_2 \cdot \mathbf{d}_0} + e^{-i\mathbf{G}_3 \cdot \mathbf{d}_0}), \quad (3)$$

where w is a tunneling strength parameter. It is informative to highlight three high-symmetry displacement values: $\mathbf{d}_{0,n} = n(\mathbf{a}_1 + \mathbf{a}_2)/3$ for $n = 0, \pm 1$, where $\mathbf{a}_{1,2}$ are the primitive translation vectors of the aligned bilayer: $\mathbf{a}_1 = a_0(1, 0)$ and $\mathbf{a}_2 = a_0(1/2, \sqrt{3}/2)$. For $n = 0$ the metal atoms of the two layers are aligned, $\Delta_{\mathbf{t}} = \Delta_{\mathbf{b}} = 6V \cos(\psi)$ and $\Delta_T = 3w$; the valence band maximum states are then symmetric and antisymmetric combinations of the isolated layer states. For $n = \pm 1$ the metal atoms in one layer are aligned with the chalcogen atoms in the other layer, and Δ_T vanishes as a result of the threefold rotational symmetry \hat{C}_{3z} . We determine the model parameters by fitting the eigenvalues of $\mathcal{H}_\uparrow(\mathbf{k} = 0)$ at the three displacements to corresponding values from

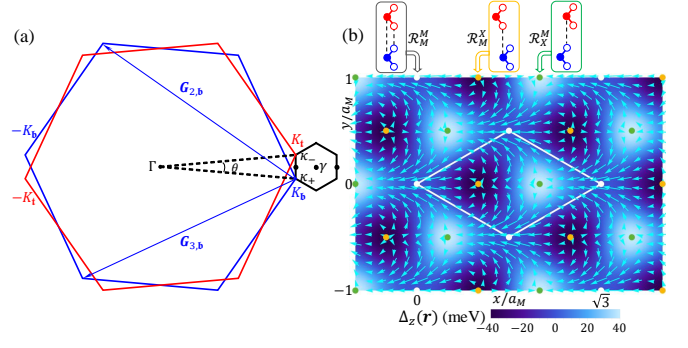


FIG. 2. (a) Brillouin zones of the bottom (blue) and top (red) layers in a twisted bilayer, and the moiré Brillouin zone (black). (b) The $+K$ -valley layer pseudospin skyrmion lattice in the moiré pattern. The color map illustrates the variation of Δ_z , and the arrows indicate $\Delta_{x,y}$. The white lines outline a single moiré unit cell. The dots indicate the high symmetry positions \mathcal{R}_M^M , \mathcal{R}_X^M and \mathcal{R}_M^X , where the local interlayer displacements are respectively $\mathbf{d}_{0,0}$, $\mathbf{d}_{0,1}$ and $\mathbf{d}_{0,-1}$.

fully relativistic band structure calculations using Quantum Espresso [19]. We find that $(V, \psi, w) \approx (8 \text{ meV}, -89.6^\circ, -8.5 \text{ meV})$ for MoTe_2 .

Moiré Hamiltonian.— We construct the twisted bilayer Hamiltonian by starting from an aligned bilayer with $\mathbf{d}_0 = 0$ and then rotating the bottom and top layers by angles $-\theta/2$ and $+\theta/2$ around a metal site. (Any initial displacement just shifts the moiré pattern globally [7, 20].) We take the origin of coordinates to be on this rotation axis and midway between layers. With respect to this origin, the bilayer has D_3 point group symmetry generated by the threefold rotation \hat{C}_{3z} around \hat{z} axis and a twofold rotation \hat{C}_{2y} around \hat{y} axis that swaps the two layers. In a long-period moiré pattern, the local displacement between the two layers, approximated by $\theta\hat{z} \times \mathbf{r}$, varies smoothly with the spatial position \mathbf{r} [18, 21]. The moiré Hamiltonian is

$$\mathcal{H}_\uparrow = \begin{pmatrix} -\frac{\hbar^2(\mathbf{k}-\boldsymbol{\kappa}_+)^2}{2m^*} + \Delta_{\mathbf{b}}(\mathbf{r}) & \Delta_T(\mathbf{r}) \\ \Delta_T^\dagger(\mathbf{r}) & -\frac{\hbar^2(\mathbf{k}-\boldsymbol{\kappa}_-)^2}{2m^*} + \Delta_{\mathbf{t}}(\mathbf{r}) \end{pmatrix}, \quad (4)$$

where $\Delta_\alpha(\mathbf{r})$ is obtained by replacing \mathbf{d}_0 in Eqs. (2)-(3) with $\theta\hat{z} \times \mathbf{r}$ to account for the spatial variation of the local inter-layer coordination. The moiré Hamiltonian is periodic with the moiré period $a_M = a_0/\theta$. Because of the twist, the $+K$ points associated with the bottom and top layers are rotated to different momenta, accounted for by the $\boldsymbol{\kappa}_\pm$ shifts in (4). We choose a moiré Brillouin zone (MBZ) in which the $\boldsymbol{\kappa}_\pm$ points are located at the MBZ corners, as illustrated in Fig. 2(a).

To reveal the spatial structure of the Δ_α field, we define the layer pseudospin magnetic field:

$$\boldsymbol{\Delta}(\mathbf{r}) = (\Delta_x, \Delta_y, \Delta_z) \equiv (\text{Re}\Delta_T^\dagger, \text{Im}\Delta_T^\dagger, \frac{\Delta_{\mathbf{b}} - \Delta_{\mathbf{t}}}{2}). \quad (5)$$

As illustrated in Fig. 2(b), $\Delta_z(\mathbf{r})$ vanishes along the links

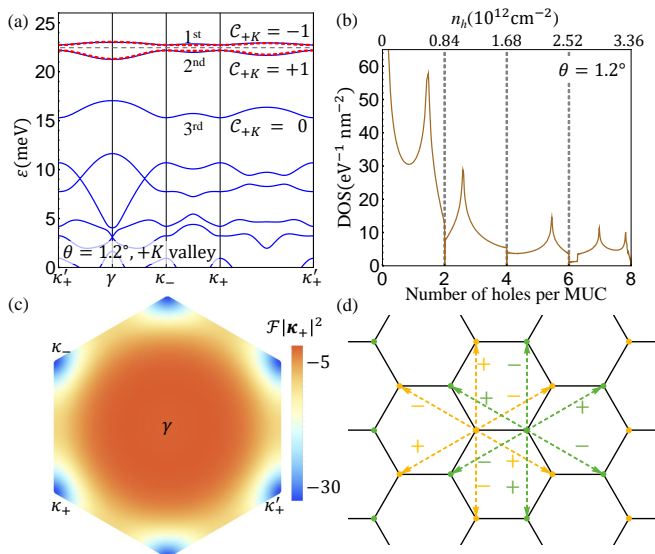


FIG. 3. (a) Moiré band structure at twist angle 1.2° . The system is a topological insulator when the chemical potential (black dashed line) is in the gap between the first and the second bands. The red dashed lines are a tight-binding-model fit based on the effective Hamiltonian (7) with $t_0 \approx 0.29$ meV and $t_1 \approx 0.06$ meV. (b) Total density of states (DOS) as a function of the number of holes per moiré unit cell (bottom) and per area (top). (c) Berry curvature \mathcal{F} for the first band in (a). Here the typical magnitude of \mathcal{F} is three orders of magnitude larger than that in the monolayer [16, 17]. (d) Illustration of the tight-binding model (7). The yellow and green dots represent \mathcal{R}_M^X and \mathcal{R}_M^M sites, and together form a honeycomb lattice. The signs \pm refer to the bond and spin dependent hopping phase factors $\exp(\pm i2\pi s/3)$.

that connect nearest-neighbor \mathcal{R}_M^M sites and has minimum and maximum values at \mathcal{R}_M^X and \mathcal{R}_M^M . The in-plane pseudospin field, which accounts for interlayer tunneling, has vortex and antivortex structures centered on \mathcal{R}_M^X and \mathcal{R}_M^M . Here \mathcal{R}_α^β denotes high-symmetry sites at which α atoms of the bottom layer are locally aligned with β atoms of the top layer. It follows that $\Delta(\mathbf{r})$ forms a skyrmion lattice, *i.e.*, that the direction of the $\Delta(\mathbf{r})$ covers the unit sphere once in each moiré unit cell (MUC). We have explicitly confirmed this property by numerically evaluating the winding number [22]:

$$N_w \equiv \frac{1}{4\pi} \int_{\text{MUC}} d\mathbf{r} \frac{\Delta \cdot (\partial_x \Delta \times \partial_y \Delta)}{|\Delta|^3} = -1. \quad (6)$$

Skyrmion lattice pseudospin textures in position space indicate [23] the possibility of topological electronic bands in momentum space, although we will find that the connection is not one-to-one.

Topological bands. — The moiré band structure is illustrated in Fig. 3(a) for a representative angle $\theta = 1.2^\circ$. The $\hat{C}_{2y}\hat{T}$ symmetry of the Hamiltonian maps $\kappa_+ \rightarrow \kappa_-$ and therefore enforces degeneracy between these points. For the two topmost moiré bands of the $+K$ valley, wave

functions in the \mathbf{b} (\mathbf{t}) layer are concentrated near the \mathcal{R}_M^M (\mathcal{R}_M^X) sites, which are Δ_b (Δ_t) maxima. Because of the layer-dependent momentum shifts κ_\pm in the kinetic energies, the moiré band wave functions vary rapidly over the MBZ. In particular, the wave function of the topmost moiré band at κ_+ and κ_- are respectively localized in layers \mathbf{b} and \mathbf{t} . By integrating the Berry curvature \mathcal{F} over the MBZ [24], we confirm that the Chern numbers \mathcal{C} of the two topmost $+K$ valley moiré bands in Fig. 3 are non-trivial ($\mathcal{C} = \pm 1$) at $\theta = 1.2^\circ$. The corresponding bands at the $-K$ valley must have the opposite Chern numbers due to the \hat{T} symmetry. Spin-valley locking implies that when the chemical potential is in the gap between the two topmost bands, the twisted homobilayer is not only a valley Hall insulator but also a quantum spin Hall insulator, *i.e.*, a topological insulator [25, 26].

To gain deeper insight into the topological bands, we construct a tight binding model. The real space distribution of the wave functions suggests a two-orbital model for the first two moiré bands:

$$H_{\text{TB}} = \sum_{\ell, s} \sum_{\mathbf{R}\mathbf{R}'} t_0 c_{\mathbf{R}\ell s}^\dagger c_{\mathbf{R}'(-\ell)s} + \sum_{\ell, s} \sum_{\mathbf{R}} \sum_{\mathbf{a}_M} t_1 e^{is\kappa_\ell \cdot \mathbf{a}_M} c_{(\mathbf{R}+\mathbf{a}_M)\ell s}^\dagger c_{\mathbf{R}\ell s}, \quad (7)$$

where $s = \pm$ denotes spin (equivalent to valley $\pm K$), and $\ell = \pm$ labels orbitals localized in the bottom (+1) and top (-1) layers and centered around the \mathcal{R}_M^X and \mathcal{R}_M^M sites. The two orbitals form a honeycomb lattice in Fig. 3(d). In (7), the spin up and down sectors are decoupled due to the spin-valley $U(1)$ symmetry of the low-energy theory, and are related by \hat{T} symmetry. The first line of (7) captures inter-layer hopping between nearest neighbors on the honeycomb lattice. Its form is constrained by the requirements that the energy spectra have threefold rotational symmetry and be identical at κ_+ and κ_- points. The second line of (7) captures intralayer hopping between next nearest neighbors on the honeycomb lattice; the bond and spin-dependent phase factors $\exp(is\kappa_\ell \cdot \mathbf{a}_M)$, which take values of $\exp(\pm i2\pi/3)$, are analogous to the Peierls substitution and account for the momentum shift κ_ℓ in (4). The Hamiltonian (7) is equivalent to the Kane-Mele model [25, 26], and to two time-reversed-partner copies of the Haldane model [27]. It correctly captures both the topological character and the energy dispersion of the first two bands in Fig. 3(a).

Beyond a critical angle $\theta_1^* \approx 1.74^\circ$ the gap between the second and the third bands closes at the γ point, as illustrated in Fig. 4. When θ crosses θ_1^* from below, the Chern number of the first band in $+K$ valley remains as -1 , while the Chern numbers for the second and third bands change from $(+1, 0)$ to $(-1, +2)$. Although, the two-orbital model (7) is not fully applicable for $\theta > \theta_1^*$ it still captures the main character of the first two bands

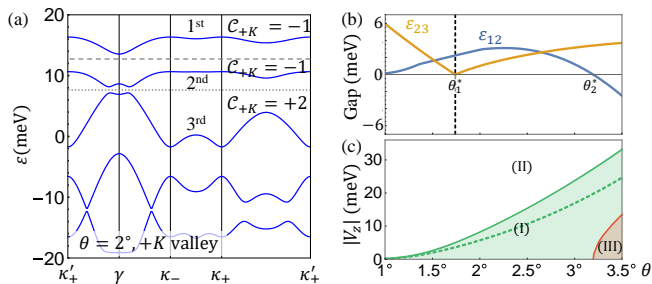


FIG. 4. (a) Moiré bands at twist angle 2° . (b) Energy gaps between adjacent moiré bands as a function of θ . The gap ε_{ij} is the difference between the minimum energy of band i and the maximum energy of band j . (c) Phase diagram as a function of angle θ and layer bias potential V_z . When the chemical potential is in the gap between the first and the second band, the system is a topological insulator in region (I) and a trivial insulator in region (II). In region (III), the two bands overlap in energy. The solid and dashed green lines show the critical bias potentials obtained using the full moiré Hamiltonian and the effective tight-binding model respectively. (b) and (c) have the same horizontal axis.

in regions of momentum space away from the γ point. The system remains as a topological insulator when the chemical potential is in the gap between the first and the second bands until θ reaches $\theta_2^* \approx 3.1^\circ$, beyond which there is no global gap between the first two bands. In the SM[17], we have verified the robustness of our predicted topological bands against perturbation from remote bands.

Field induced topological transition.— Because the two sublattices in (7) are associated with different layers, a vertical electric field generates a staggered sublattice potential, which can induce a topological phase transition [25–27]. To study this transition, we add a layer dependent potential $\ell V_z/2$ to the moiré Hamiltonian (4) so that $\Delta_z \rightarrow (\Delta_b - \Delta_t + V_z)/2$. (We neglect the small spatial modulation of V_z due to variation in the vertical distance between layers in the moiré pattern [28].) The magnitude of V_z has a critical value $|V_z|_c$, at which the gap between the first and the second moiré bands closes at κ_\pm points. When $|V_z| > |V_z|_c$, wave functions in the first moiré band are primarily localized in one single layer and the band becomes topologically trivial. The tight-binding model (7) predicts that $|V_z|_c$ is equal to splitting between the first and the second bands at κ_\pm when $V_z = 0$, because the interlayer hopping term in (7) vanishes at these momenta. In Fig. 4(c) we compare values of $|V_z|_c$ calculated from the tight-binding and the full moiré band Hamiltonian, showing that they match well, particularly for small twist angles (long moiré period). We note that there is no one-to-one correspondence between the Chern numbers \mathcal{C} of the electronic bands and the winding number N_w of the pseudospin field, which remains non-trivial until V_z equals $|\Delta_b - \Delta_t|$ evaluated at the \mathcal{R}_M^X or \mathcal{R}_X^M sites.

Interaction effects.— When the moiré bands are nearly

flat, the density of states is strongly enhanced [Fig. 3(b)] and many-body interaction effects are magnified. Here we focus on interaction effects within the first two moiré bands at zero V_z and small θ . The on-site Coulomb repulsion U_0 scales as $e^2/(\epsilon a_W)$, where ϵ is an effective dielectric constant that depends on the three-dimensional dielectric environment, and a_W is the spatial extent of the Wannier orbitals centered at \mathcal{R}_M^X or \mathcal{R}_X^M sites. For θ around 1° , we find that U_0 can be more than one order of magnitude larger than the hopping parameters $t_{0,1}$ [17]. In the strong correlation limit, we anticipate that the interplay between layer and spin/valley degrees of freedom will lead to unusual distinct insulating states at integer numbers of holes per MUC. For one hole per MUC, where the first moiré band is half filled, one candidate insulating state is ferromagnetic. Because the single-particle Hamiltonian has only $U(1)$ symmetry, perpendicular spin polarization is energetically preferred. The Ising spin anisotropy implies finite temperature phase transitions. When the first moiré band is completely spin-polarized, the system is a quantum anomalous Hall insulator. Similar physics could occur for three holes per MUC, where the second moiré band is half filled. For two holes per MUC (equivalently one hole per sublattice site of the honeycomb lattice in Kane-Mele model), there is a competition between the quantum spin Hall insulator and the antiferromagnetic insulator [29], which occur for weak and strong interactions respectively. For some fractional numbers of holes per MUC, the flat bands may host fractional topological insulators [30].

Discussion.— It has been proposed that Hubbard model can be simulated in TMD *heterobilayers* [10]. In twisted TMD *homobilayers*, the two layers can be effectively decoupled by using a finite layer bias potential to drive the system into region (II) of the phase diagram in Fig. 4(c). Thus, conventional one-orbital Hubbard model can also be studied in twisted homobilayers, with a greater scope for *in situ* manipulation of model parameters. Compared to heterobilayers, twisted TMD homobilayers may be experimentally realized with a more precise control of the twist angle by using the ‘tear-and-stack’ technique [4, 8, 9]. In the SM [17], we also show that a two-orbital Hubbard model can be simulated using twisted TMD homobilayers in the AB stacking configuration. Moiré bands with valley-contrasting Chern numbers have been proposed in some graphene-based moiré systems [14, 15, 31]. In this case however, quantum spin Hall states that might be induced by interactions cannot survive to accessible temperatures because electrons in graphene have accurate $SU(2)$ spin symmetry which enhances fluctuation effects. In Ref. [32], quantum spin Hall nano-dots and nano-strips have been proposed for TMD-based moiré systems in which the large gap between valence and conduction bands needs to be inverted by strong vertical electric field. In contrast, our model Hamiltonian relies only on valence band states. Our pro-

posals for topological states is based on valley contrast physics and on pseudospin texture in the moiré pattern; the advantage is that it does not require massless chiral fermions in the parent monolayer or aligned bilayer, which may lead to application in a larger class of two-dimensional materials.

F.W. and I.M. are supported by the Department of Energy, Office of Science, Materials Science and Engineering Division. F.W. is also supported by Laboratory for Physical Sciences. Work at Austin is supported by Army Research Office (ARO) Grant W911NF-17-1-0312 (MURI) and by the Welch foundation under Grant TBF1473. We acknowledge HPC resources provided by the Texas Advanced Computing Center (TACC) at The University of Texas at Austin.

-
- [1] B. Hunt, J. D. Sanchez-Yamagishi, A. F. Young, M. Yankowitz, B. J. LeRoy, K. Watanabe, T. Taniguchi, P. Moon, M. Koshino, P. Jarillo-Herrero, and R. C. Ashoori, *Science* **340**, 1427 (2013).
- [2] C. R. Dean, L. Wang, P. Maher, C. Forsythe, F. Ghahari, Y. Gao, J. Katoch, M. Ishigami, P. Moon, M. Koshino, T. Taniguchi, K. Watanabe, K. L. Shepard, J. Hone, and P. Kim, *Nature* **497**, 598 (2013).
- [3] L. Wang, Y. Gao, B. Wen, Z. Han, T. Taniguchi, K. Watanabe, M. Koshino, J. Hone, and C. R. Dean, *Science* **350**, 1231 (2015).
- [4] K. Kim, A. DaSilva, S. Huang, B. Fallahazad, S. Larentis, T. Taniguchi, K. Watanabe, B. J. LeRoy, A. H. MacDonald, and E. Tutuc, *Proc. Natl. Acad. Sci. U.S.A.* **114**, 3364 (2017).
- [5] E. M. Spanton, A. A. Zibrov, H. Zhou, T. Taniguchi, K. Watanabe, M. P. Zaletel, and A. F. Young, *Science* **360**, 62 (2018).
- [6] G. Chen, L. Jiang, S. Wu, B. Lv, H. Li, K. Watanabe, T. Taniguchi, Z. Shi, Y. Zhang, and F. Wang, *arXiv:1803.01985* (2018).
- [7] R. Bistritzer and A. H. MacDonald, *Proc. Natl. Acad. Sci. U.S.A.* **108**, 12233 (2011).
- [8] Y. Cao, V. Fatemi, A. Demir, S. Fang, S. L. Tomarken, J. Y. Luo, J. D. Sanchez-Yamagishi, K. Watanabe, T. Taniguchi, E. Kaxiras, R. C. Ashoori, and P. Jarillo-Herrero, *Nature* **556**, 80 (2018).
- [9] Y. Cao, V. Fatemi, S. Fang, K. Watanabe, T. Taniguchi, E. Kaxiras, and P. Jarillo-Herrero, *Nature* **556**, 43 (2018).
- [10] F. Wu, T. Lovorn, E. Tutuc, and A. H. MacDonald, *Phys. Rev. Lett.* **121**, 026402 (2018).
- [11] H. C. Po, L. Zou, A. Vishwanath, and T. Senthil, *Phys. Rev. X* **8**, 031089 (2018).
- [12] F. Wu, A. H. MacDonald, and I. Martin, *Phys. Rev. Lett.* **121**, 257001 (2018).
- [13] M. H. Naik and M. Jain, *Phys. Rev. Lett.* **121**, 266401 (2018).
- [14] B. L. Chittari, G. Chen, Y. Zhang, F. Wang, and J. Jung, *Phys. Rev. Lett.* **122**, 016401 (2019).
- [15] Y.-H. Zhang, D. Mao, Y. Cao, P. Jarillo-Herrero, and T. Senthil, *arXiv:1805.08232* (2018).
- [16] D. Xiao, G.-B. Liu, W. Feng, X. Xu, and W. Yao, *Phys. Rev. Lett.* **108**, 196802 (2012).
- [17] See Supplemental Material at URL for ab initio band structure, perturbations from remote bands, additional discussion of interaction effects, and simulation of two-orbital Hubbard model using the AB stacking configuration, which includes Ref. [33–35].
- [18] J. Jung, A. Raoux, Z. Qiao, and A. H. MacDonald, *Phys. Rev. B* **89**, 205414 (2014).
- [19] P. Giannozzi *et al.*, *J. Phys.: Condens. Matter* **21**, 395502 (2009).
- [20] F. Wu, T. Lovorn, and A. H. MacDonald, *Phys. Rev. B* **97**, 035306 (2018).
- [21] F. Wu, T. Lovorn, and A. H. MacDonald, *Phys. Rev. Lett.* **118**, 147401 (2017).
- [22] K. Moon, H. Mori, K. Yang, S. M. Girvin, A. H. MacDonald, L. Zheng, D. Yoshioka, and S.-C. Zhang, *Phys. Rev. B* **51**, 5138 (1995).
- [23] N. Nagaosa and Y. Tokura, *Nature Nanotechnology* **8**, 899 (2013).
- [24] D. Xiao, M.-C. Chang, and Q. Niu, *Rev. Mod. Phys.* **82**, 1959 (2010).
- [25] C. L. Kane and E. J. Mele, *Phys. Rev. Lett.* **95**, 226801 (2005).
- [26] C. L. Kane and E. J. Mele, *Phys. Rev. Lett.* **95**, 146802 (2005).
- [27] F. D. M. Haldane, *Phys. Rev. Lett.* **61**, 2015 (1988).
- [28] C. Zhang, C.-P. Chuu, X. Ren, M.-Y. Li, L.-J. Li, C. Jin, M.-Y. Chou, and C.-K. Shih, *Sci. Adv.* **3**, e1601459 (2017).
- [29] M. Hohenadler, T. C. Lang, and F. F. Assaad, *Phys. Rev. Lett.* **106**, 100403 (2011).
- [30] X.-L. Qi, *Phys. Rev. Lett.* **107**, 126803 (2011).
- [31] J. C. W. Song, P. Samutpraphoot, and L. S. Levitov, *Proc. Natl. Acad. Sci. U.S.A.* **112**, 10879 (2015).
- [32] Q. Tong, H. Yu, Q. Zhu, Y. Wang, X. Xu, and W. Yao, *Nat. Phys.* **13**, 356 (2017).
- [33] G.-B. Liu, W.-Y. Shan, Y. Yao, W. Yao, and D. Xiao, *Phys. Rev. B* **88**, 085433 (2013).
- [34] M. K. Agarwal and M. J. Capers, *J. Appl. Cryst.* **5**, 63 (1972).
- [35] Y. Wang, Z. Wang, W. Yao, G.-B. Liu, and H. Yu, *Phys. Rev. B* **95**, 115429 (2017).

Supplemental Material

This Supplemental Material includes the following five sections: (1) DFT band structure, (2) a four-band model with remote conduction bands, (3) a four-band model with remote spin-split valence bands, (4) interaction effects in the Kane-Mele model, and (5) simulation of two-orbital Hubbard model using the AB stacking configuration where the two layers are relatively rotated by an angle near π .

DFT BAND STRUCTURE

We perform fully-relativistic density functional theory (DFT) calculations under the local density approximation (LDA) for aligned MoTe₂ bilayers using Quantum Espresso [19]. The Perdew-Zunger (LDA) exchange-correlation functional has been used. We choose a plane-wave cutoff energy of 50 Ry and a corresponding charge density cutoff energy of 408 Ry, and we sample the Brillouin zone with a $16 \times 16 \times 1$ grid of k points. The thickness of the vacuum layer is about 20 Å. The in-plane lattice constant a_0 is taken to be 3.472 Å. [33, 34] The in-plane atomic positions are fixed, while the out-of-plane positions have been relaxed for all atoms until the out-of-plane direction force on each atom is less than 0.005 eV/Å.

The band structures for AA stacked MoTe₂ bilayers ($\theta = 0$) are shown in Figs. 5(a, b) respectively for in-plane displacements $\mathbf{d}_{0,0}$ and $\mathbf{d}_{0,1}$. We note that bilayers with displacements $\mathbf{d}_{0,1}$ and $\mathbf{d}_{0,-1}$ are related by a mirror operation $z \leftrightarrow -z$; therefore the two structures have identical energy dispersion, while the wave function characters are related by the mirror operation. We measure the layer separation by the vertical distance D_z between the metal (Mo) atoms associated with different layers. With this definition, D_z is respectively 7.8 Å and 6.9 Å for $\mathbf{d}_{0,0}$ and $\mathbf{d}_{0,1}$ structures.

As shown in Fig. 5, the valence band maxima are located in $\pm K$ valleys for both $\mathbf{d}_{0,0}$ and $\mathbf{d}_{0,1}$ structures. Therefore, in our model study, the topmost moiré valence states are derived from $\pm K$ valleys. This is the reason why we choose MoTe₂ bilayers, whereas in other TMDs, for example MoS₂ bilayers [13], the valence band maximum is located in Γ valley. Because the valence band maximum at the Γ point is only lower in energy compared to that at $\pm K$ points by about 80 meV in the $\mathbf{d}_{0,1}$ structure of MoTe₂, the DFT calculation may not be accurate enough to precisely determine the energy separation between Γ and $\pm K$ valence states. However, the Γ and $\pm K$ states are always separated by a large momentum, and therefore, they can be studied separately in a low-energy theory.

To determine the orbital, layer and spin characters of the bands, we obtain a tight-binding Hamiltonian in a

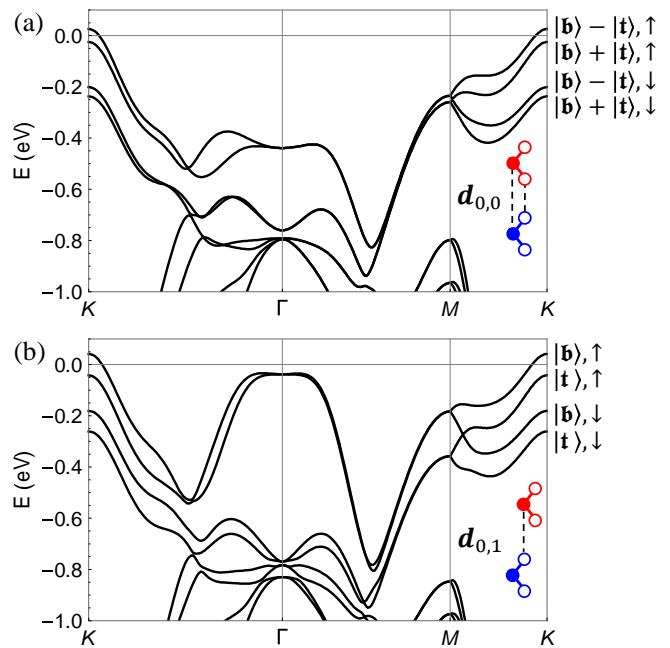


FIG. 5. DFT band structure for AA stacked MoTe₂ bilayers with $\theta = 0$. The in-plane displacement between the two layers are $\mathbf{d}_{0,0}$ in (a) and $\mathbf{d}_{0,1}$ in (b). The major layer and spin characters of the valence bands at $+K$ point are listed, which are fully consistent with our analytic model. The zero energy is taken to be the same as that in Eq. (1) of the main text.

basis of Wannier functions using Wannier90. We project onto p orbitals of Te and d orbitals of Mo without performing maximal localization, and reproduce the DFT band structure with high accuracy.

We have also performed DFT study for AA stacked WSe₂ bilayer, of which the valence band maxima are located at $\pm K$ points for $\mathbf{d}_{0,0}$ structure, but at Γ point for $\mathbf{d}_{0,\pm 1}$ structures, according to our calculation. Because of this complicated energy landscape, it should be examined experimentally whether low-energy moiré bands in twisted bilayer WSe₂ are derived from $\pm K$ valleys or Γ valley. More advanced band structure calculation, such as GW calculation, should also be applied to bilayer WSe₂ to get a more accurate estimation of the energy landscape. The effective model in Eq.(2) of the main text applies equally to $+K$ valley moiré valence states in twisted bilayer WSe₂ (other TMDs as well); the corresponding parameter values for WSe₂ are $(V, \psi, w) \approx (8.9 \text{ meV}, 91^\circ, 9.7 \text{ meV})$, and there are similar topological moiré bands.

REMOTE CONDUCTION BANDS

In monolayer TMDs, the $k.p$ Hamiltonian at $\pm K$ valleys is often described by a massive Dirac model in the basis of conduction and valence band states [16]. This

massive Dirac model is particularly convenient for analyses of the valley dependent optical selection rules. In the main text, we have discarded the conduction band states and used a parabolic band approximation for valence band states. There is a question about whether such an approximation is adequate to capture all important low-energy physics, in particular the moiré band structure and the topological character. Below we answer this question in the affirmative by studying a moiré Hamiltonian that includes both the valence and conduction bands.

As in the main text, we study spin up states at $+K$ valley. For aligned bilayers, the $k.p$ Hamiltonian that includes both conduction and valence band states is given by:

$$\mathcal{H}_\uparrow(\theta = 0, \mathbf{d}_0) = \begin{pmatrix} h_b(\mathbf{k}, \mathbf{d}_0) & T(\mathbf{d}_0) \\ T^\dagger(\mathbf{d}_0) & h_t(\mathbf{k}, \mathbf{d}_0) \end{pmatrix}, \quad (8)$$

where h_ℓ is the massive Dirac Hamiltonian in layer ℓ , and $T(\mathbf{d}_0)$ is the interlayer tunneling matrix. h_ℓ is given by:

$$h_\ell(\mathbf{k}, \mathbf{d}_0) = \begin{pmatrix} \Delta_g + \Delta_{\ell,c}(\mathbf{d}_0) & \hbar v_F(k_x - ik_y) \\ \hbar v_F(k_x + ik_y) & \Delta_{\ell,v}(\mathbf{d}_0) \end{pmatrix}. \quad (9)$$

Here the two components refer to the metal d_{z^2} and $d_{x^2-y^2} + id_{xy}$ orbital states, which carry different angular momenta and represent the main character respectively for conduction (c) and valence (v) band states. In (9), Δ_g is the average band gap, $\Delta_{\ell,\xi}(\mathbf{d}_0)$ is the variation of band ξ extrema energy as a function of \mathbf{d}_0 , and v_F is the Fermi velocity. Here ξ is the band index for c and v . Similar to Eq.(2) in the main text, $\Delta_{\ell,\xi}$ can be parametrized as:

$$\Delta_{\ell,\xi}(\mathbf{d}_0) = 2V_\xi \sum_{j=1,3,5} \cos(\mathbf{G}_j \cdot \mathbf{d}_0 + \ell\psi_\xi). \quad (10)$$

The tunneling matrix $T(\mathbf{d}_0)$ is derived by using a two-center approximation [7] and also taking into account the threefold-rotational symmetry at high-symmetry displacements [35]. $T(\mathbf{d}_0)$ is parametrized as:

$$\begin{aligned} T(\mathbf{d}_0) &= \begin{pmatrix} w_c & w_{cv} \\ w_{vc} & w_v \end{pmatrix} \\ &+ \begin{pmatrix} w_c & w_{cv}e^{-i2\pi/3} \\ w_{vc}e^{i2\pi/3} & w_v \end{pmatrix} e^{-i\mathbf{G}_2 \cdot \mathbf{d}_0} \\ &+ \begin{pmatrix} w_c & w_{cv}e^{i2\pi/3} \\ w_{vc}e^{-i2\pi/3} & w_v \end{pmatrix} e^{-i\mathbf{G}_3 \cdot \mathbf{d}_0}. \end{aligned} \quad (11)$$

The mirror operation ($z \leftrightarrow -z$) leads to the constraints that w_c and w_v are real numbers, and $w_{cv} = w_{vc}^*$. Note that the interlayer tunneling between valence and conduction band states vanishes at $\mathbf{d}_0 = 0$.

We determine parameter values by fitting to the first-principles band structure at the three high-symmetry displacements. For AA stacked MoTe_2 bilayer, we obtain that $\Delta_g = 1.1$ eV, $v_F = 0.4 \times 10^6$ m/s, $(V_v, \psi_v, w_v) =$

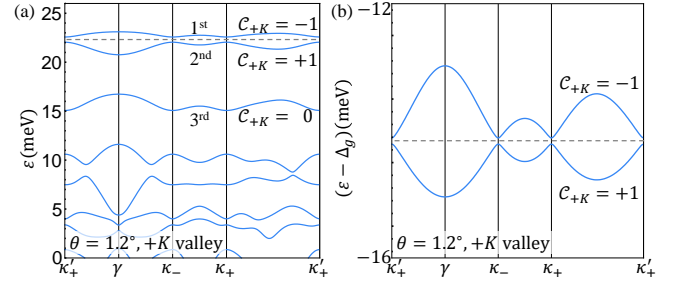


FIG. 6. Moiré band structure obtained from the four-band model in (12). The twist angle is 1.2° . (a) Moiré valence bands. (b) Two lowest energy moiré conduction bands in spin up sector at $+K$ valley. Note that the energy is measured relative to Δ_g in (b).

(8 meV, -89.6° , -8.5 meV), $(V_c, \psi_c, w_c) = (5.97$ meV, -87.9° , -2 meV) and $w_{cv} = 15.3$ meV. Here ψ_v and ψ_c are close to -90° , which implies that the scalar potential $(\Delta_{b,\xi} + \Delta_{t,\xi})/2$ has an amplitude much smaller than that of the potential difference $(\Delta_{b,\xi} - \Delta_{t,\xi})/2$. We note that density-functional theory underestimates the band gap Δ_g , but the exact numerical values should not influence qualitative effects that we discuss.

The band gap Δ_g is much larger than other energy scales. Therefore, we can integrate out conduction band states using a second-order perturbation theory, and the resulting model is exactly that in Eq. (1) of the main text. The effective mass m^* is then approximated by $\Delta_g/(2v_F^2)$, and the spatial modulation of m^* is of order $V_\xi/\Delta_g \ll 1$ and can be neglected. In the main text, $m^* = 0.62m_e$ has been used where m_e is the electron bare mass. This provides the first justification that the model with only valence band states is valid.

We continue with the four-band Hamiltonian (8). When there is a twist between the two layers, the moiré Hamiltonian is:

$$\mathcal{H}_\uparrow = \begin{pmatrix} h_b(\mathbf{k}, \mathbf{r}) & T(\mathbf{r}) \\ T^\dagger(\mathbf{r}) & h_t(\mathbf{k}, \mathbf{r}) \end{pmatrix}, \quad (12)$$

where \mathbf{r} is the two-dimensional position operator. h_ℓ in the moiré pattern has the form

$$\begin{aligned} h_\ell(\mathbf{k}, \mathbf{r}) &= \begin{pmatrix} \Delta_g + \Delta_{\ell,c}(\mathbf{r}) & 0 \\ 0 & \Delta_{\ell,v}(\mathbf{r}) \end{pmatrix} \\ &+ e^{-i\ell\frac{\theta}{4}\xi_z} [\hbar v_F(\mathbf{k} - \boldsymbol{\kappa}_\ell) \cdot \boldsymbol{\xi}] e^{+i\ell\frac{\theta}{4}\xi_z}, \end{aligned} \quad (13)$$

where $\boldsymbol{\xi}$ is the Pauli matrix in the band basis. The moiré potentials $\Delta_{\ell,\xi}(\mathbf{r})$ and the tunneling term $T(\mathbf{r})$ are obtained from Eqs. (10)-(11) by replacing \mathbf{d}_0 with $\theta\hat{z} \times \mathbf{r}$. The moiré Hamiltonian (12) is formally similar to that for twisted bilayer graphene [7, 12], and the main differences are the Dirac mass Δ_g .

We diagonalize the moiré Hamiltonian (12) by using a plane-wave expansion and parameter values of MoTe_2 bilayer. The moiré bands and the Chern numbers are

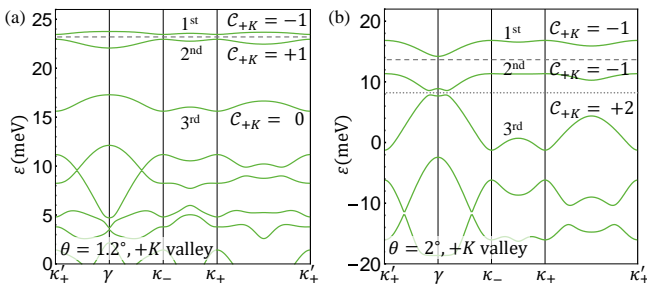


FIG. 7. Moiré band structure obtained from the four-band model in (14) that includes spin mixing effects. The twist angle is 1.2° in (a) and 2° in (b). The bands shown in these figures are mainly of spin up character, while spin down bands are separated from them by $\Delta_{SOC} \sim 220$ meV.

summarized in Fig. 6. The moiré valence bands and the Chern numbers are consistent with those obtained using the two-band model of the main text. Fig. 6(b) shows the two lowest-energy moiré conduction bands in spin up sector at $+K$ valley, which carry Chern numbers ± 1 . The topological character of the moiré conduction bands can be understood in the same way as that for valence bands.

In monolayer TMD, the valence band edges at valley $\pm K$ already carry a finite Berry curvature due to the absence of inversion symmetry [16], and the corresponding Berry curvature at $+K$ point is given by $-2(\hbar v_F/\Delta_g)^2$, which is about -0.113 nm² for monolayer MoTe₂. In contrast, the typical value of the Berry curvature as shown in Fig. 3 of the main text for the topological moiré band is about $-10/|\kappa_+|^2 \approx -156.6$ nm², three orders of magnitude larger than the intrinsic monolayer value. We can define a dimensionless quantity $2(\hbar v_F|\kappa_+|/\Delta_g)^2 \sim 7 \times 10^{-3}$, which is much smaller than 1 and justifies the two-band model with only valence band sates.

REMOTE VALENCE BANDS

We study spin mixing effects from remote valence bands. In TMDs, the topmost spin up and down valence bands at $\pm K$ points are separated in energy by more than 100 meV. In monolayer TMDs, the $z \leftrightarrow -z$ mirror symmetry can be used to classify the bands into two mirror sectors, and the spin-mixing effects are typically ignored. In bilayer TMDs, this mirror symmetry is generally broken.

Here we study valence bands at $+K$ valley, including spin-orbit split bands. For aligned bilayers, the $k \cdot p$ Hamiltonian is given by:

$$\mathcal{H}(\theta = 0, \mathbf{d}_0) = \begin{pmatrix} h_b(\mathbf{k}, \mathbf{d}_0) & T(\mathbf{d}_0) \\ T^\dagger(\mathbf{d}_0) & h_t(\mathbf{k}, \mathbf{d}_0) \end{pmatrix}, \quad (14)$$

Here h_ℓ is the intra-layer Hamiltonian given by:

$$h_\ell = \begin{pmatrix} -\frac{\hbar^2 \mathbf{k}^2}{2m^*} + \Delta_{\ell\uparrow}(\mathbf{d}_0) & 0 \\ 0 & -\Delta_{SOC} - \frac{\hbar^2 \mathbf{k}^2}{2m^*} + \Delta_{\ell\downarrow}(\mathbf{d}_0) \end{pmatrix}, \quad (15)$$

where the two components refer to spin up and down valence states at valley $+K$. Here we use up and down to refer to the major spin character. In (15), the off-diagonal spin-mixing terms are approximated as zero because these terms vanish at the three high-symmetry displacements $\mathbf{d}_{0,n}$ due to the three-fold rotational symmetry. Δ_{SOC} is the spin splitting, and the variation energy $\Delta_{\ell s}$ is parametrized as:

$$\Delta_{\ell s}(\mathbf{d}_0) = 2V_s \sum_{j=1,3,5} \cos(\mathbf{G}_j \cdot \mathbf{d}_0 + \ell\psi_s). \quad (16)$$

The interlayer tunneling does include symmetry-allowed spin-mixing terms:

$$T(\mathbf{d}_0) = \begin{pmatrix} w_\uparrow & w_{\uparrow\downarrow} \\ w_{\downarrow\uparrow} & w_\downarrow \end{pmatrix} + \begin{pmatrix} w_\uparrow & w_{\uparrow\downarrow} e^{-i2\pi/3} \\ w_{\downarrow\uparrow} e^{i2\pi/3} & w_\downarrow \end{pmatrix} e^{-i\mathbf{G}_2 \cdot \mathbf{d}_0} + \begin{pmatrix} w_\uparrow & w_{\uparrow\downarrow} e^{i2\pi/3} \\ w_{\downarrow\uparrow} e^{-i2\pi/3} & w_\downarrow \end{pmatrix} e^{-i\mathbf{G}_3 \cdot \mathbf{d}_0}. \quad (17)$$

The mirror operation ($z \leftrightarrow -z$), which maps \mathbf{d}_0 to $-\mathbf{d}_0$, implies that w_\uparrow and w_\downarrow are real, and $w_{\uparrow\downarrow} = -w_{\downarrow\uparrow}^*$, because the mirror operation acts as $-is_z$ in the spin space and ℓ_x in the layer space. Note that this mirror operation is not a symmetry for a generic \mathbf{d}_0 except at $\mathbf{d}_0 = \mathbf{0}$.

We again determine the parameter values by fitting to the first-principles band structure, and obtain that $\Delta_{SOC} = 220.5$ meV, $(V_\uparrow, \psi_\uparrow, w_\uparrow) = (8$ meV, $-89.6^\circ, -8.5$ meV), $(V_\downarrow, \psi_\downarrow, w_\downarrow) = (7.7$ meV, $-88.35^\circ, -6$ meV) and $w_{\uparrow\downarrow} = -i5.6$ meV.

We map the Hamiltonian in (14) to the moiré Hamiltonian at a finite twist angle. The calculated moiré band structure are shown in Fig. 7, which are nearly identical to that obtained in the main text. This is expected because the spin mixing terms are at least an order of magnitude smaller compared to the spin-orbit splitting Δ_{SOC} .

In conclusion, the two-band model given in Eq. (1) of the main text provides a faithful low-energy description of moiré valence bands at small twist angles. We have used quantum spin Hall insulator as a synonym of two-dimensional topological insulator [26], which is a distinct phase without requirement of spin conservation.

In our theory, spin, strictly speaking, is not a good quantum number, but valley is a good quantum number and plays the role of an effective spin. Therefore, the Z_2 invariant of the quantum spin Hall insulator and the valley Chern number are directly connected. We can denote the Chern number for bands below a chemical potential in valley τK as $\mathcal{C}_{\tau K}$, where τ is $+$ or

– for the two valleys. Because of time-reversal symmetry, $C_{+K} = -C_{-K}$. The Z_2 invariant is given by $[(C_{+K} - C_{-K})/2] \bmod 2 = C_{+K} \bmod 2$. Based on this definition, the system is in the quantum spin Hall insulator phase (two-dimensional time-reversal-invariant topological insulator) in region (I) of Fig. 4(c) [main text] when the chemical potential is in the gap between the first and the second moiré bands.

KANE-MELE-HUBBARD MODEL

We provide additional discussion of many-body interactions in the topological moiré bands. As in the main text, we focus on interaction effects within the first two moiré bands with small twist angle, where the tight-binding model H_{TB} is applicable.

The interaction strength can be tuned by the three-dimensional dielectric environment, and the range of interaction can be controlled by a nearby metallic gate. Here we only consider the on-site repulsive interaction U_0 and assume that longer-range interactions are suppressed due to the nearby gate. Effects of long-range Coulomb interaction on the topological bands are also interesting, which we leave to future exploration. U_0 scales as $e^2/(\epsilon a_W)$, where ϵ is the effective dielectric constant. a_W is the spatial extent of the Wannier orbitals, which can be estimated based on a harmonic oscillator potential approximation of the moiré potential $\Delta_\ell(\mathbf{r})$ near one of its maximum position [10]. At $\theta = 1.2^\circ$, a_W is about 3 nm; for comparison, the corresponding moiré period a_M is 16.6 nm. If we take ϵ to be 10, then $U_0 \approx e^2/(\epsilon a_W) \approx 47$ meV, which is two orders of magnitude larger than the hopping parameter $t_0 \approx 0.29$ meV at $\theta = 1.2^\circ$. Therefore, the ratio U_0/t_0 , which depends on the dielectric environment and the twist angle, can be much greater than one.

By combining the tight-binding model and the on-site interaction, we arrive at the Kane-Mele-Hubbard model:

$$H = H_{\text{TB}} + U_0 \sum_{\mathbf{R}\ell} n_{\mathbf{R}\ell\uparrow} n_{\mathbf{R}\ell\downarrow}. \quad (18)$$

The tight-binding model is given by:

$$\begin{aligned} H_{\text{TB}} &= \sum_{\ell,s} \sum_{\mathbf{R}\mathbf{R}'} t_0 c_{\mathbf{R}\ell s}^\dagger c_{\mathbf{R}'(-\ell)s} \\ &+ \sum_{\ell,s} \sum_{\mathbf{R}} \sum_{\mathbf{a}_M} t_1 e^{i\mathbf{s}\mathbf{K}\ell \cdot \mathbf{a}_M} c_{(\mathbf{R}+\mathbf{a}_M)\ell s}^\dagger c_{\mathbf{R}\ell s}, \\ &= \sum_{\mathbf{k}} c_{\mathbf{k}}^\dagger [f_0 + f_z \sigma_z s_z + f_x \sigma_x + f_y \sigma_y] c_{\mathbf{k}}, \end{aligned} \quad (19)$$

where $\sigma_{x,y,z}$ and $s_{x,y,z}$ are Pauli matrices in the sublattice and spin spaces, and $f_{0,x,y,z}$ are functions of the momentum \mathbf{k} . The tight binding model has two energy

branches $f_0 \pm \sqrt{f_x^2 + f_y^2 + f_z^2}$ and each branch is doubly degenerate. The term f_0 is not important for the topological properties and is absent in the original Kane-Mele model of Refs. [25, 26]. At the filling factor where there are two electrons per unit cell (equivalent to one electron per sublattice site), there is a competition between the quantum spin Hall insulator and the antiferromagnetic Mott insulator in the Kane-Mele-Hubbard model [29]. Here we focus on a different filling factor where there are three electrons (equivalent to one hole) per unit cell. At this filling factor, the upper two bands are half filled in the non-interacting limit. Because the upper two bands carry spin contrast Chern numbers, the isolated upper band in either spin sector does not have exponentially localized Wannier states. These nearly flat topological bands are similar to Landau levels which are completely flat but have no exponentially localized Wannier states. It is well established that Landau levels with internal degeneracies (for example spin) develop ferromagnetism when they are partially filled with an integer number of electrons per cyclotron orbit. By making an analogy to the Landau level problems, we anticipate that ferromagnetism is likely at the filling factor of one hole per moiré unit cell.

We now use a mean-field theory to demonstrate the Ising anisotropy in the ferromagnetic state. We perform a Hartree-Fock approximation for the Hubbard interaction on each site:

$$n_\uparrow n_\downarrow \approx \frac{n_0^2 + \mathbf{m}^2}{4} - \frac{1}{2} c^\dagger (\mathbf{m} \cdot \mathbf{s}) c \quad (20)$$

where $n_0 = \langle n_\uparrow + n_\downarrow \rangle$ and $\mathbf{m} = \langle c^\dagger \mathbf{s} c \rangle$. Here $\langle \dots \rangle$ represents the mean-field average value, and $n_0 = 3/2$. The full mean-field Hamiltonian is:

$$\begin{aligned} H_{\text{MF}} &= 2\mathcal{N} \frac{M^2}{U_0} \\ &+ \sum_{\mathbf{k}} c_{\mathbf{k}}^\dagger [f_0 + f_z \sigma_z s_z + f_x \sigma_x + f_y \sigma_y + \mathbf{M} \cdot \mathbf{s}] c_{\mathbf{k}}, \end{aligned} \quad (21)$$

where $\mathbf{M} = -U_0 \mathbf{m}/2$, and \mathcal{N} is the number of unit cells. H_{MF} generally has four non-degenerate energy bands. We consider zero temperature, and assume that the magnetization is strong enough such that the highest energy band is completely empty and other three bands are fully occupied by electrons. The total energy is then given by:

$$\begin{aligned} \mathcal{E}(\mathbf{M}) &= \text{constant} + 2\mathcal{N} \frac{M^2}{U_0} \\ &- \sum_{\mathbf{k}} \sqrt{M^2 + \mathbf{f}^2 + 2|M| \sqrt{\mathbf{f}_\perp^2 + f_z^2} \cos^2 \theta_{\mathbf{M}}}, \end{aligned} \quad (22)$$

where $\mathbf{f}^2 = \mathbf{f}_\perp^2 + f_z^2$, $\mathbf{f}_\perp^2 = f_x^2 + f_y^2$, and the vector \mathbf{M} is parametrized by the spherical coordinates $M(\sin \theta_{\mathbf{M}} \cos \phi_{\mathbf{M}}, \sin \theta_{\mathbf{M}} \sin \phi_{\mathbf{M}}, \cos \theta_{\mathbf{M}})$. The saddle

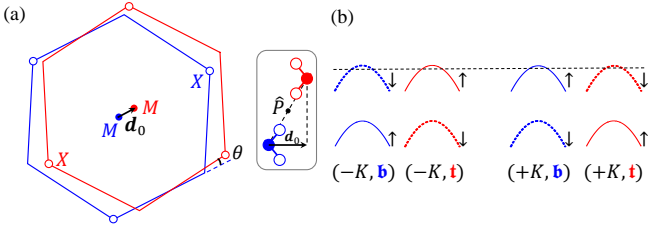


FIG. 8. (a) AB stacked TMD MX_2 homobilayer. The inset schematically shows the side view at zero twist angle, where the black dot on the dashed line is an inversion center. (b) Schematic plot of the valence bands at $\pm K$ valleys in the AB stacked homobilayer.

point equation $\partial\mathcal{E}/\partial\mathbf{M} = 0$ correctly reproduces the self-consistent equation $\mathbf{m} = \langle c^\dagger \mathbf{s} c \rangle$. The energy functional $\mathcal{E}(\mathbf{M})$ is independent of the azimuthal angle $\phi_{\mathbf{M}}$, which is a result of the spin $U(1)$ symmetry of the Hamiltonian (18). $\mathcal{E}(\mathbf{M})$ does depend on the polar angle $\theta_{\mathbf{M}}$, and is minimized by placing \mathbf{M} along \hat{z} axis. Thus, there is an Ising anisotropy that favors the out-of-plane spin polarization.

AB STACKING CONFIGURATION

In TMD bilayers with long period moiré pattern, there is another distinct stacking configuration that we label as AB [20]. AA and AB stacking, which are sometimes respectively referred to as R and H stacking, are distinguished by a 180° rotation of the top layer. Below we discuss $\pm K$ valley moiré bands in the AB stacking configuration.

In AB stacking with zero twist angle and an arbitrary in-plane displacement \mathbf{d}_0 , there is always an inversion symmetry \hat{P} , and the inversion center is at the midpoint between the two shifted metal atoms located in different layers [35], as illustrated in Fig. 8. The combined symmetry $\hat{P}\hat{T}$ enforces a double degeneracy of the band structure at every momentum. We again focus on $+K$ valley, and electronic properties at $-K$ valley can be inferred by using the \hat{T} symmetry. At $+K$ valley, the topmost

valence bands associated with the bottom and top layer respectively have spin up and down characters, and they are degenerate due to the $\hat{P}\hat{T}$ symmetry, leading to the following $k.p$ Hamiltonian:

$$\mathcal{H}_{+K}(\theta = 0, \mathbf{d}_0) = \begin{pmatrix} -\frac{\hbar^2 \mathbf{k}^2}{2m^*} + \Delta(\mathbf{d}_0) & 0 \\ 0 & -\frac{\hbar^2 \mathbf{k}^2}{2m^*} + \Delta(\mathbf{d}_0) \end{pmatrix}, \quad (23)$$

where the two components refer to bottom (spin up) and top (spin down) layers, $\Delta(\mathbf{d}_0)$ is the variation of the valence band maximum energy as a function of \mathbf{d}_0 , and the 2×2 Hamiltonian is proportional to an identity matrix in the layer pseudospin space because of the $\hat{P}\hat{T}$ symmetry. In this low-energy Hamiltonian (23), the two layers are effectively decoupled.

In twisted bilayer, we obtain the moiré Hamiltonian by replacing \mathbf{d}_0 with $\theta \hat{z} \times \mathbf{r}$ and taking into account the momentum shift between the two layers:

$$\mathcal{H}_{+K} = \begin{pmatrix} -\frac{\hbar^2 (\mathbf{k} - \boldsymbol{\kappa}_+)^2}{2m^*} + \Delta(\mathbf{r}) & 0 \\ 0 & -\frac{\hbar^2 (\mathbf{k} - \boldsymbol{\kappa}_-)^2}{2m^*} + \Delta(\mathbf{r}) \end{pmatrix}, \quad (24)$$

where the two layers are again effectively decoupled and can be studied separately in the single particle Hamiltonian, and the momentum shift $\boldsymbol{\kappa}_\pm$ can therefore be removed by a layer-dependent gauge transformation. In each layer electrons move in the layer-independent potential $\Delta(\mathbf{r})$ and form moiré bands that are topologically trivial. The topmost moiré valence bands can be used to simulate the Hubbard model on a triangular lattice with two orbitals that are centered in different layers but at the same in-plane positions. This two-orbital Hubbard model has an approximate $SU(4)$ symmetry, which would become exact if the vertical separation between the two orbitals were neglected. We will report a detailed study of this two-orbital Hubbard model in a separate work. A vertical electric field generates an energy difference between the two orbitals, and can lead to the realization of the conventional single-orbital Hubbard model when the field is strong enough [10].